Available online at www.sciencedirect.com

ScienceDirect

journal homepage: www.elsevier.com/locate/he

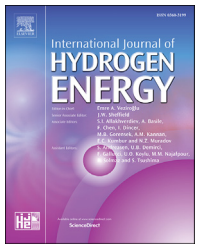

DFT simulation of hydrogen storage on manganese phosphorous trisulphide ($MnPS_3$)

I. Cabria [a,*], *A.A. El-Meligi* [b]

[a] *Departamento de Física Teórica, Atómica y Óptica, Universidad de Valladolid, 47011 Valladolid, Spain*
[b] *Department of Math. and Science, AMA International University – Bahrain, Bahrain and National Research Center, Egypt*

ARTICLE INFO

Article history:
Received 31 August 2017
Received in revised form
10 October 2017
Accepted 16 October 2017
Available online 8 November 2017

Keywords:
Hydrogen storage
Hydrogen physisorption
Layered materials
Transition metal phosphorous trisulphides
DFT

ABSTRACT

Manganese phosphorous trisulphide, $MnPS_3$, is a solid layered material. The hydrogen gravimetric storage capacities of $MnPS_3$ powder at 80.15, 173.15 and 298.15 K and at moderate pressures has been recently measured in experiments. The origin of the storage capacities of this material is not well understood. The main hypothesis is that hydrogen is stored in the pores of $MnPS_3$ powder. The pores are modelled as two parallel $MnPS_3$ layers separated a certain distance. Density Functional Theory simulations of the interaction of H_2 with the surface of a $MnPS_3$ layer have been carried out, in order to test that hypothesis. The simulations indicate that the adsorption of hydrogen on the surface of a $MnPS_3$ layer is energetically favourable, but only through the physisorption mechanism. Calculations of the gravimetric capacities of the pores of $MnPS_3$ powder have also been carried out, obtaining a reasonable agreement with the experimental results. The comparison of the calculated and experimental gravimetric capacities show that the hydrogen storage on $MnPS_3$ powder is mainly due to compression in the pores and that the contribution of the physisorption process to the storage is very small.

Introduction

Hydrogen is a candidate to replace fossil fuels in future cars. The current technology involves storing hydrogen of two ways: In tanks either as compressed gas at high pressures, up to 70 MPa, or liquefied under cryogenic temperatures, below 30 K. These processes have drawbacks for transportation applications: There is a need for energy to compress gas at high pressures or to liquefy hydrogen and this increase the cost [1,2]. A third way is the storage in a solid material. Hydrogen can be stored in a solid material through different mechanisms: physisorption, chemisorption and chemical reactions. Many solid materials have been investigated to store hydrogen through physisorption, such as, metallic-organic frameworks (MOFs), organic polymers, carbon nanotubes and nanoporous carbons [3–32].

Transition metal trichalcogenophosphates are a set of solid layered materials with the structure MPX_3 (where M = transition metal, Mn, Fe, Zn, etc., and X = S or Se). These materials are used as nonlinear optical materials, catalytic materials, magnetic materials and cathode materials in the rechargeable batteries [33–36] and have a huge potential for spintronic devices [37–39]. The wide range of applications of these materials is due to their structure, electric and magnetic properties, which have been studied extensively [33,39–43]. However, the

* *Corresponding author.*
E-mail address: ivan.cabria@uva.es (I. Cabria).
https://doi.org/10.1016/j.ijhydene.2017.10.103

hydrogen storage capacities of these layered materials have barely been investigated. Recently, the capacities of $MnPS_3$, $FePS_3$ and $MgPS_3$ powder to store hydrogen at moderate pressures and at low and room temperatures has been measured in experiments [44–46]. The main hypothesis is that hydrogen molecules are stored in the pores of the powder of these materials, but the storage mechanisms are not well understood.

Dispersion interactions are an important contribution to the interaction of H_2 with a surface. These interactions are not included in the local density approximation (LDA) and the generalized gradient approximation (GGA) versions of the density functional theory (DFT). In the last fifteen years, different DFT-based methods including dispersion interactions have been developed and tested in many dispersion-dominated systems [47,48].

The novelty of the present work is to use DFT calculations that include the dispersion interactions to explain the hydrogen gravimetric storage capacities of $MnPS_3$ powder, measured in recent experiments by Ismail et al. [45]. Computer simulations of hydrogen storage on nanoporous carbons, MOFs and clusters have been performed [5,12,13,49–68], but to our knowledge, these are the first DFT calculations of the hydrogen gravimetric storage capacities of layered materials of the type MPS_3. To explain the experimental capacities, DFT calculations of the interaction of H_2 (chemisorption and physisorption) on a single $MnPS_3$ layer have been carried out, and the hydrogen gravimetric storage capacities of the pores of $MnPS_3$ powder have been calculated using the DFT results and a quantum-thermodynamic model applied in former papers to nanoporous carbons [52,56,58,59,69]. Comparisons between the experimental and theoretical gravimetric storage capacities are made and conclusions are extracted from that comparison.

Research methodology

Method

DFT calculations of a single $MnPS_3$ layer and of H_2 on a single $MnPS_3$ layer were performed using the BigDFT code [70–72], which uses a systematic wavelet basis set. The parameters to select the basis wavelets were chosen in such a way that the physisorption energy of H_2 on the surface of a single $MnPS_3$ layer is accurate within 0.1 meV.

The exchange-correlation functional used for the calculations is the Perdew, Burke, and Ernzerhof (PBE) approximation [73], and the pseudopotentials used are the dispersion corrected atom-centered nonlocal pseudopotentials (DCACPs) developed by Rothlisberger and co-workers [74–78]. These calculations are named PBE + DCACP throughout this paper. The parameters of these pseudopotentials were obtained by fitting the values of the properties of weakly bonded dimers of H_2, benzene, N_2, CO_2, He, Ne, Ar and Kr [77,78] to the results of high-level first principles calculations. The results obtained with the DCACPs on different systems indicate that the dispersion forces can be well described within the DFT-GGA with the DCACP approach. These pseudopotentials represent an alternative to include the dispersion forces within the DFT framework.

Geometric structure of $MnPS_3$

According to the experiments, $MnPS_3$ is a solid layered material with a monoclinic unit cell that it is almost orthorhombic [45,79–83]. The experimental values of the *a*, *b* and *c* lattice parameters are a = 6.076, 10.524 and 6.796 Å, respectively, and the angle β is 107.35°. The experimental geometric structure of bulk $MnPS_3$ is depicted in Fig. 1. Three single $MnPS_3$ layers have been plotted in that figure. A single $MnPS_3$ layer is composed of three shells: The central shell is made of Mn atoms in an hexagonal array, and the other two shells (above and below the central one) are made of PS_3 units (See Fig. 1). The two external surfaces of a $MnPS_3$ layer are made of sulphur atoms. The empty space between two adjacent $MnPS_3$ layers in bulk $MnPS_3$ is called the Van der Waals gap in the literature. The experimental value of the Van der Waals gap is 3.5 Å. This gap is too narrow and does not allow to store molecules by physisorption mechanism between the $MnPS_3$ layers of $MnPS_3$ bulk.

A single $MnPS_3$ layer has been used to represent the open surface of $MnPS_3$. The single $MnPS_3$ layer was simulated by applying surface periodic conditions to the unit cell depicted in Fig. 2, which contains four $MnPS_3$ units. This unit cell has only *a* and *b* lattice parameters, because it is a unit cell with surface periodic conditions. The geometry of the single $MnPS_3$ layer has been optimized. The lattice parameters *a* and *b* of the unit cell and the positions of all the atoms of the unit cell were optimized. Geometries are considered optimized when the forces on the atoms are less than 0.002 eV/Å. The optimized values of the lattice parameters of the unit cell of the single $MnPS_3$ layer obtained in the PBE + DCACP calculations are a = 5.69 and b = 11.00 Å.

According to the experiments, $MnPS_3$ is an antiferromagnetic material with two antiferromagnetic arrangements or phases called type I and II, both depicted in Fig. 3, and the magnetic moment on Mn is 5 μ_B [80,84]. In type II, each Mn^{2+} ion of the hexagons interacts antiferromagnetically with its three nearest Mn^{2+} neighbours in the Mn layer.

Spin-polarized calculations have been performed, studying different magnetic arrangements of the magnetic moments of the atoms of the unit cell of $MnPS_3$, in particular, the ferromagnetic arrangement and the two experimental antiferromagnetic arrangements, shown in Fig. 3, and different values of the magnetic moment on the Mn^{2+} ions. For the purpose of

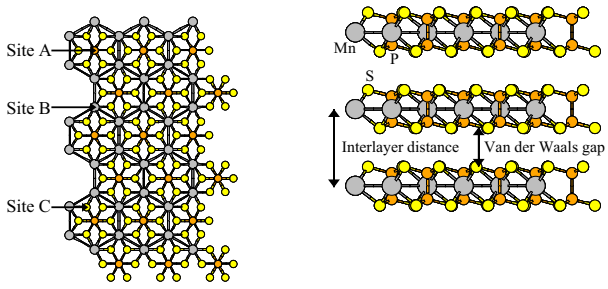

Fig. 1 – Top and lateral views of bulk $MnPS_3$. Mn, P and S atoms are the gray, orange and yellow balls, respectively. (For interpretation of the references to colour in this figure legend, the reader is referred to the web version of this article.)

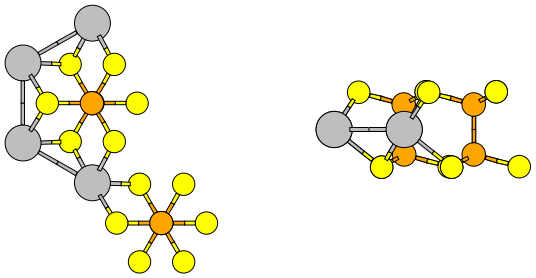

Fig. 2 – Top and lateral views of the unit cell of the single $MnPS_3$ layer used to simulate the surface of $MnPS_3$. Mn, P and S atoms are the gray, orange and yellow balls, respectively. (For interpretation of the references to colour in this figure legend, the reader is referred to the web version of this article.)

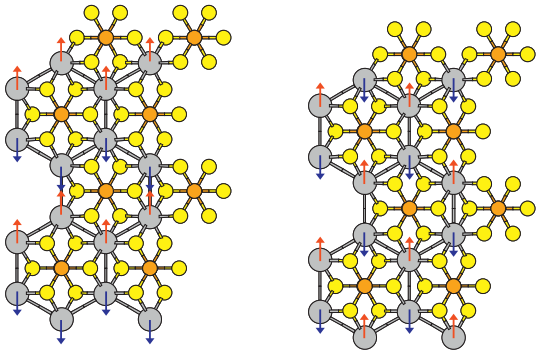

Fig. 3 – Type I (left) and type II (right) antiferromagnetic structures of the $MnPS_3$ layered material. Mn, P and S atoms are the gray, orange and yellow balls, respectively. (For interpretation of the references to colour in this figure legend, the reader is referred to the web version of this article.)

visualization, the magnetic moments on the Mn^{2+} ions are depicted in Fig. 3 as lying on the plane of the layer, but in real they are perpendicular to the layer plane. According to the present calculations, the most stable structure was the type II structure with 5 μ_B on Mn. The difference in energy between the type II and the other magnetic arrangements is about 0.1 eV/unit cell. Therefore, the type II structure was chosen to make the calculations of the $MnPS_3$ layer. The optimization of the geometry of the $MnPS_3$ layer, explained in the former section, was carried out using the type II antiferromagnetic structure.

Results and discussion

Interaction of H_2 with the surface of the $MnPS_3$ layer

PBE + DCACP calculations of the chemisorption and physisorption of H_2 on a single $MnPS_3$ layer have been carried out. To study the chemisorption, the relaxation of the geometric positions of the two hydrogen atoms and their nearest S and P atoms of the unit cell of the $MnPS_3$ layer on sites A, B and C, was allowed. The locations of sites A, B and C on the $MnPS_3$ layer are depicted in Fig. 1. Sites A, B and C are on top of P, Mn and S atoms, respectively. These are the sites with the highest symmetry. The energies and geometries of the chemisorbed states obtained are summarized in Table 1. The binding energy, in the case of chemisorption, is defined according to the equation:

$$E_b = E(2H\ on\ MnPS_3\ layer) - E(H_2) - E(MnPS_3\ layer). \quad (1)$$

It can be seen in Table 1 that the binding energies E_b of the chemisorbed states, calculated using Eq. (1), are positive, which means that these states are less stable than the isolated H_2 molecule and the $MnPS_3$ layer. Therefore, these states can not contribute to a reversible hydrogen storage.

As shown in Table 1, there is a relationship between E_b and d_{HH}: As the binding energy E_b increases, the H–H distance decreases. However, the H–S distance remains approximately constant. Physisorption of hydrogen was simulated by placing the molecule on top of sites A, B and C of the surface layer and varying the H_2-surface distance. For each site, calculations were done for two orientations of the molecular axis of H_2 with respect to the surface: perpendicular and parallel. Therefore, six configurations of H_2 physisorbed on a single $MnPS_3$ layer were studied. The physisorption binding energy $E_b(d)$ of H_2 was defined according to the equation:

$$E_b(d) = E(H_2\ on\ MnPS_3\ layer; d) - E(H_2) - E(MnPS_3\ layer)\ , \quad (2)$$

where $E(H_2\ on\ MnPS_3\ layer; d)$ is the energy of the system composed by H_2 on the surface of a $MnPS_3$ layer and at a distance d from the surface of the layer.

The equilibrium H_2-surface distances, d_e, and the minimum binding energies, $E_b(d_e)$, of the six configurations obtained in the PBE + DCACP calculations, are shown in Table 2. $E_b(d_e)$ is calculated from Eq. (2), with $d = d_e$.

The most stable physisorption configuration, according to the results in Table 2, consists on the molecule on site A with the axis of the H_2 molecule parallel to the surface. That configuration has the lowest value of $E_b(d_e)$, −0.025 eV, and is plotted in Fig. 4. The physisorption binding energy $E_b(d)$, Eq. (2), as a function of the H_2-surface distance d obtained in the present PBE + DCACP calculations for that configuration, is also shown in Fig. 5.

The minimum binding energies $E_b(d_e)$ of the six configurations in Table 2 are negative and therefore, the molecule is bonded to the surface of a $MnPS_3$ layer on the six configurations. These are very weak energies and this is qualitatively consistent with the low hydrogen storage gravimetric capacities of $MnPS_3$, measured in the experiments [45]. The results of the present calculations of H_2 on a $MnPS_3$ layer, indicate that the adsorption and storage of H_2 on the surface of $MnPS_3$ is energetically favourable, but the storage capacity is very

Table 1 – Binding energies, E_b, (in eV/molecule), H–H distance, d_{HH}, and average H–S distance, d_{HS}, (in Å) of the chemisorbed hydrogen states on the $MnPS_3$ layer surface.

Site	E_b	d_{HH}	d_{HS}
A	2.76	1.71	1.36
B	2.47	1.99	1.37
C	1.54	2.02	1.35

Table 2 – Equilibrium H_2-surface distances, d_e, in Å, and minimum binding energies, $E_b(d_e)$, in eV, for H_2 physisorbed on three sites of the $MnPS_3$ layer surface and for two orientations of the molecular axis.

Site	Orientation	d_e	$E_b(d_e)$
A	Parallel	3.4	−0.025
A	Perpendicular	3.6	−0.018
B	Parallel	3.4	−0.022
B	Perpendicular	3.3	−0.022
C	Parallel	3.7	−0.018
C	Perpendicular	3.6	−0.019

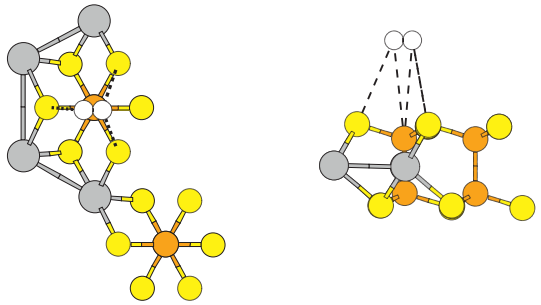

Fig. 4 – Top and lateral views of the unit cell used in the calculations of H_2 interacting with a $MnPS_3$ layer. H, Mn, P and S atoms are the white, gray, orange and yellow balls, respectively. H_2 is on site A and parallel to the layer surface. (For interpretation of the references to colour in this figure legend, the reader is referred to the web version of this article.)

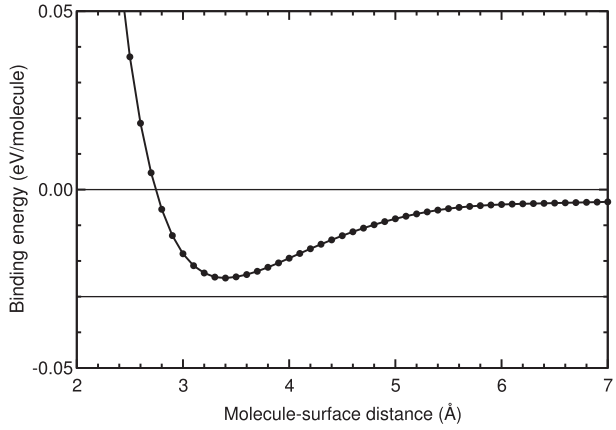

Fig. 5 – Physisorption binding energy of H_2 on a $MnPS_3$ layer surface, as a function of the H_2-surface distance. Results were obtained in PBE + DCACP calculations, with the molecule on top of site A and parallel to the surface.

small because the interaction of H_2 with the surface of $MnPS_3$ is very weak.

These are qualitative conclusions about the storage capacity of $MnPS_3$. In order to obtain quantitative conclusions, it is necessary to calculate the gravimetric storage capacities of $MnPS_3$ and to compare them with the storage capacities reported in the experiments [45]. This is explained and discussed in the next section.

Hydrogen storage on the pores of $MnPS_3$ powder

A quantum-thermodynamic model, based on the Van't Hoff equation of the equilibrium between the compressed and adsorbed phases of hydrogen [52,56], was applied in previous investigations [56,58,59,69] to calculate the hydrogen storage capacities of nanoporous carbons simulated as graphene slit, cylindrical and spherical pores. The physisorption energy curve of a H_2 molecule on the surface of the pores was obtained from DFT calculations. Slit pores were simulated as planar parallel graphene layers. Cylindrical and spherical pores were simulated as the inner cavities of nanotubes and fullerenes, respectively. This model gives results consistent with the experimental storage capacities of activated carbons (ACs) [23,27] and carbide-derived carbons (CDCs) [17,24,26,28], and allows us to make predictions of the optimal width of slit pores. In this paper, the quantum-thermodynamic model is applied to the pores of $MnPS_3$ powder, performing extensive simulations to study the dependence of the hydrogen storage capacities on the pore size, the pressure and the temperature.

To apply the quantum-thermodynamic model, first the geometric shape of the pores of the $MnPS_3$ powder should be chosen. According to the experiments, the reversible hydrogen storage seems to be due to the pores of the $MnPS_3$ powder. Between the layers there is not enough space to store hydrogen molecules reversibly. Therefore, a reasonable geometric model of the pores of $MnPS_3$ powder, responsible of the hydrogen storage, consists on a slit pore whose two parallel walls are single $MnPS_3$ layers. This geometric model to represent the pores of the $MnPS_3$ powder is called $MnPS_3$ slit pore throughout all this paper and has been plotted in Fig. 6. In that figure, the distance d between the internal surfaces of the layers is the size or width of the pores of the $MnPS_3$ powder.

Second, the physisorption energy curve between a H_2 molecule and the surface of a $MnPS_3$ layer is the potential $V(z)$ obtained in the PBE + DCACP calculations and plotted in the former section in Fig. 5, where z is the H_2-surface layer distance. In the $MnPS_3$ slit pore there are two $MnPS_3$ layers, and therefore the total potential is $V(z) + V(d - z)$, where d is the distance between the internal surfaces of the two layers, or the width of the pore (See Fig. 6).

The gravimetric hydrogen storage capacity in wt %, is defined as

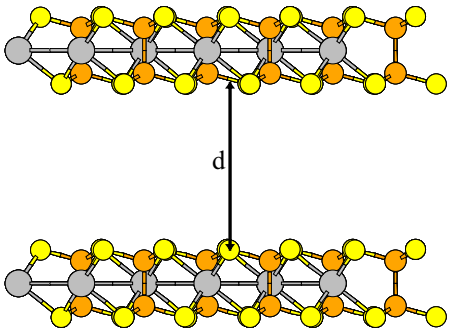

Fig. 6 – $MnPS_3$ slit pore, composed by two parallel $MnPS_3$ layers. d is the distance between the internal surfaces of the layers.

$$g_c = 100\,\frac{mass_H}{mass_H + mass_{adsorbent\ material}}\,. \quad (3)$$

This is the definition and units of the gravimetric capacities plotted in the figures of this paper. The total gravimetric capacity is calculated using the mass of the stored hydrogen or total mass, $mass_{H\,total}$, instead of $mass_H$ in Eq. (3).

The mass of stored hydrogen is the sum of the masses of the adsorbed phase and the compressed or free or bulk gas phase in a pore [85–87]. Both masses are calculated using the quantum-thermodynamic model and the basic parts mentioned above: The geometric model and the physisorption energy curve.

The two phases are depicted in Fig. 7. The adsorbed phase is the sum of the blue and purple regions and the compressed phase is the red region in Fig. 7. The masses of these two phases and the mass of stored hydrogen have been calculated using the quantum-thermodynamic model. The adsorbed phase is composed by molecules physisorbed on the surface of the pores. This phase is located on the surface of the pores (See the blue and purple regions in Fig. 7). The molecules of the purple mass are physisorbed on the surface of the pores and they are part of the adsorbed phase, but these molecules are normally present in the compressed or bulk gas phase in the same volume occupied by the adsorbed phase. The molecules of the blue mass in Fig. 7 are also physisorbed, but they are not present in the compressed or free gas phase and therefore, they are called the molecules of the excess mass. In Fig. 7 the blue and purple regions have been depicted separately to explain their different physical origins, but the molecules of these regions are mixed in the adsorbed phase. The mass of the adsorbed phase, $mass_{H\,adsorbed}$, is calculated using the Van't Hoff equation of the equilibrium between the compressed and adsorbed phases of hydrogen and the Mills-Younglove equation of state of hydrogen [52,56].

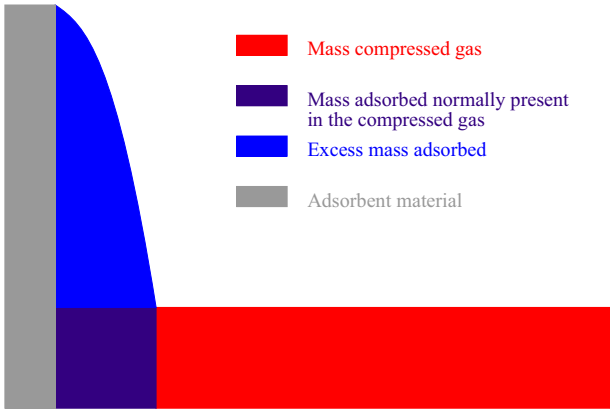

Fig. 7 – Depiction of the masses of the adsorbed and compressed phases of H_2 gas on an adsorbent material.

The compressed or bulk gas phase is composed by hydrogen molecules stored only by compression in the pores at a constant hydrogen bulk gas density. These molecules do not interact with the surface and they are not physisorbed. The mass of the compressed phase, $mass_{H\,compressed}$, is the mass of hydrogen given by the Mills-Younglove equation of state of H_2, which is part of the quantum-thermodynamic model, at the corresponding pressure and temperature, inside the volume of the $MnPS_3$ slit pore not occupied by the adsorbed phase. The mass of the compressed phase is the red mass depicted in Fig. 7.

The gravimetric capacities of the adsorbed and compressed phases are given by Eq. (3) using as $mass_H$ the mass of the adsorbed phase of hydrogen, $mass_{H\,adsorbed}$, and the mass of the compressed phase of hydrogen, $mass_{H\,compressed}$, respectively.

The theoretical gravimetric isotherms of $MnPS_3$ powder (total, adsorbed and compressed) obtained with the quantum-thermodynamic model at 80.15, 173.15 and 298.15 K are plotted and compared with the experimental gravimetric isotherms in Figs. 8 and 9. The experimental isotherms come from the experimental paper on $MnPS_3$ published by Ismail et al. [45].

It is a well-known experimental fact that at low temperatures, the contribution to the adsorption comes from all the pores and that at higher temperatures, the contribution comes mainly from the narrowest pores. Therefore, the comparison of the theoretical isotherms with the experimental ones must be done as follows: The experimental isotherms at 80.15 and 173.15 K must be compared with the

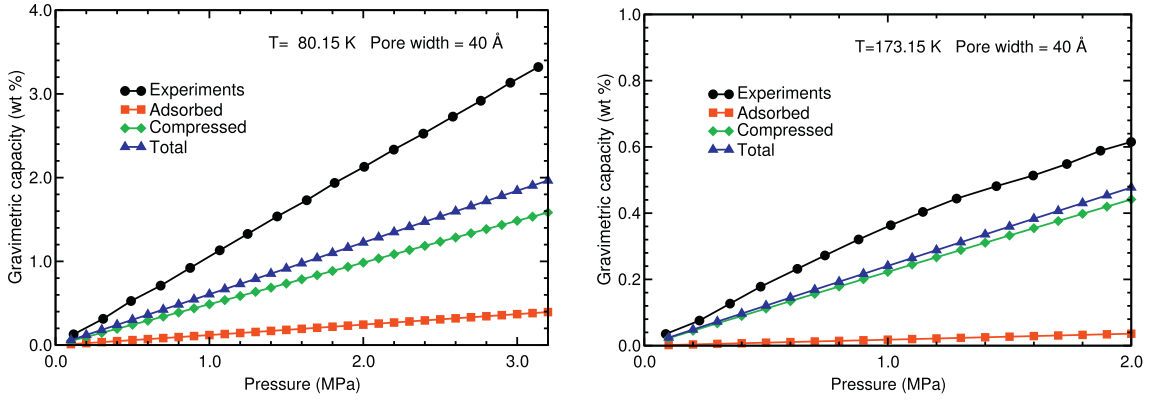

Fig. 8 – Experimental and theoretical gravimetric hydrogen storage capacities of $MnPS_3$, as a function of pressure, for 80.15 and 173.15 K, and a pore width of 40 Å.

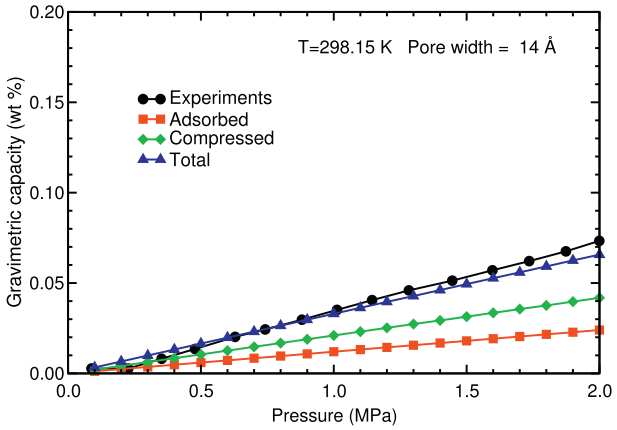

Fig. 9 – Experimental and theoretical gravimetric hydrogen storage capacities of $MnPS_3$, as a function of pressure, for 298.15 K and a pore width of 14 Å.

theoretical isotherms coming from all the pores, or equivalently, with the theoretical isotherms from the average pore size of the pores of the $MnPS_3$ powder. According to the pore size distribution of $MnPS_3$ measured by Madian et al. [88], the average size of the pores of the $MnPS_3$ powder is about 40 Å. On the other hand, the experimental isotherms at 298.15 K must be compared with the theoretical isotherms from the narrow pores of the powder, about 14 Å wide.

In the experiments on $MnPS_3$, the total gravimetric capacity was measured [45] and hence, the total gravimetric capacity is compared in Figs. 8 and 9. The theoretical curves of the gravimetric capacity due to the average pore size, 40 Å wide, agree well with the experimental curves measured at low temperatures, 80.15 and 173.15 K (See Fig. 8). The theoretical curves due to the narrow pores, 14 Å wide, agree well with the experimental curves of the total gravimetric capacity at 298.15 K (See Fig. 9).

It should be noticed that the mass of stored hydrogen or total mass of hydrogen is the sum of the masses of the adsorbed and compressed phases, but the total gravimetric capacity is not the sum of the adsorbed and compressed gravimetric capacities, due to the definition of the gravimetric capacities. The total gravimetric capacity is given by

$$g_{c\ total} = 100\ \frac{mass_{H\ total}}{mass_{H\ total} + mass_{adsorbent\ material}} = 100\ \frac{mass_{H\ adsorbed} + mass_{H\ compressed}}{mass_{H\ adsorbed} + mass_{H\ compressed} + mass_{adsorbent\ material}}. \quad (4)$$

The above definition of the total gravimetric capacity, Eq. (4), can be also written as a function of the adsorbed and

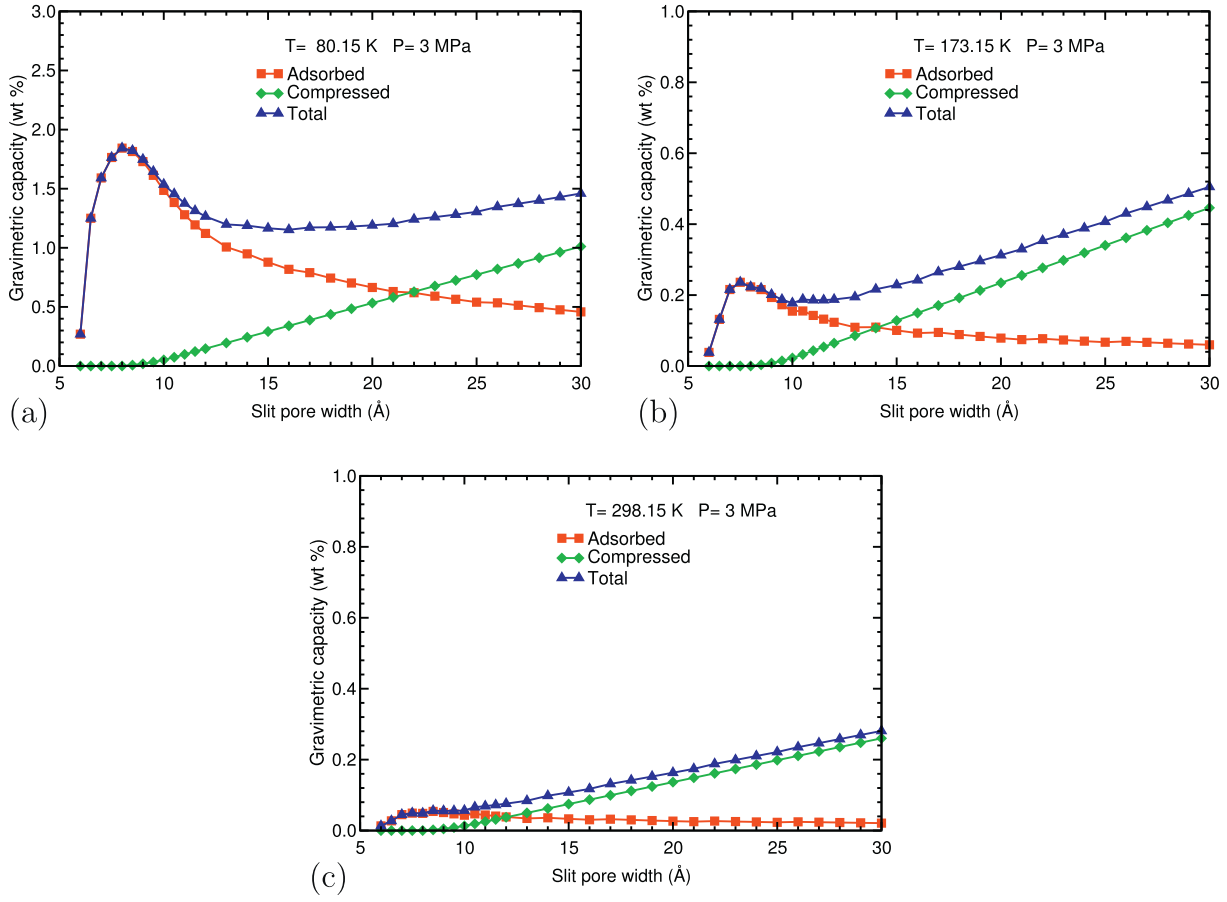

Fig. 10 – Theoretical gravimetric hydrogen storage capacities of $MnPS_3$, as a function of the pore width, at 3 MPa and temperature of (a) 80.15, (b) 173.15 and (c) 298.15 K.

compressed gravimetric capacities, $g_{c\,adsorbed}$ and $g_{c\,compressed}$, respectively:

$$g_{c\ total} = \frac{g_{c\ adsorbed} + g_{c\ compressed} - 0.02\, g_{c\ adsorbed} g_{c\ compressed}}{1 - g_{c\ adsorbed}\, 0.01\, g_{c\ compressed}\, 0.01}. \quad (5)$$

It can be seen in Eq. (5) that the total gravimetric capacity is not the sum of the adsorbed and compressed gravimetric capacities. However, the adsorbed and compressed gravimetric capacities of this material are small in the range of temperatures and pressures and pore widths studied, and therefore, the total gravimetric capacity is approximately equal to the sum of the adsorbed and compressed gravimetric capacities.

As can be noticed in Figs. 8 and 9, most of the total gravimetric capacity at the three studied temperatures, comes from the compressed gravimetric capacity and the contribution of the adsorbed gravimetric capacity is very small. In fact, the agreement between the theory and the experiments does not exist without the compressed gravimetric capacity. This is important, because it explains the experimental results: The storage capacity of $MnPS_3$ is small, the main storage mechanism is compression and the contribution of the physisorption mechanism to the storage is very small. The trend of the gravimetric capacity curves in Figs. 8 and 9 is linear, which also indicates that the main storage mechanism is compression.

Optimal hydrogen storage on $MnPS_3$ and on similar layered chalcogenides

The gravimetric storage capacities depend on the pore size. Calculations of the gravimetric storage capacities of $MnPS_3$ slit pores as a function of the $MnPS_3$ slit pore width have been carried out. The results are plotted in Fig. 10 for the three temperatures studied in the present work: 80.15, 173.15 and 298.15 K, and at a pressure of 3 MPa.

The adsorbed gravimetric capacity has a global maximum in the interval 7.5–8.5 Å of pore widths, for temperatures of 80.15 and 173.15 K, as can be seen in Fig. 10. It has not a global maximum for 298.15 K. The compressed gravimetric capacity increases linearly with the pore width and has not a global maximum for the three temperatures (See Fig. 10). The compressed gravimetric capacity is due to the molecules stored by compression in the volume of the pore, for a fixed temperature and pressure. The compressed gravimetric capacity increases linearly with the pore width. The reason of this linear increase is as follows: The volume of the pore increases linearly with the pore width and hence, also the mass of the compressed phase in the pore, which in turn causes the linear increase of the compressed gravimetric capacity.

The total capacity has a local maximum for 80.15 and 173.15 K, but not a global maximum. The local maximum is more pronounced as the temperature decreases. The total capacity has not a local maximum for 298.15 K. Therefore, for these three temperatures, there is not a pore width that yields the highest total gravimetric capacity and the total gravimetric capacity can not be optimized. The reason is that the total capacity is dominated by the compressed gravimetric capacity in the region of large pore widths, which increases linearly with the pore width, as can be seen in Fig. 10.

Conclusions

DFT calculations of the interaction of H_2 with the surface of $MnPS_3$ have shown that the adsorption on the surface is energetically possible, but only through the weak physisorption mechanism. The hydrogen gravimetric storage capacity of the pores of $MnPS_3$ powder has been simulated as a function of the temperature, the pressure and the width of the pores, using the DFT results and a quantum-thermodynamic model. There is a reasonable agreement between the experimental and theoretical gravimetric capacities. The simulations of the gravimetric capacities and its comparison with the experimental results show that most of the total gravimetric capacity comes from the compressed hydrogen phase and that the contribution from the adsorbed hydrogen phase is very small. This means that the main hydrogen storage process in the pores of $MnPS_3$ powder is compression and that the physisorption process has a very small contribution.

DFT calculations of bulk $MnPS_3$ are underway to study the intercalation and storage of H_2 molecules in the Van der Waals gap between the layers of intercalated bulk $MnPS_3$.

Acknowledgments

This work was supported by MICINN (Grant MAT2011–22781), MINECO of Spain (Grant MAT2014-54378-R), Junta de Castilla y León (Grant VA158A11-2 and VA050U14) and the University of Valladolid. I. Cabria acknowledges the facilities provided by Centro de Proceso de Datos - Parque Científico of the University of Valladolid. A. A. El-Meligi thanks his colleagues at National Research Center, Cairo, Egypt, for their support and cooperation.

REFERENCES

[1] Ren J, Musyoka NM, Langmi HW, Mathe M, Liao S. Current research trends and perspectives on materials-based hydrogen storage solutions: a critical review. Int J Hydrogen Energy 2017;42:289–311.
[2] Broom DP, Webb CJ, Hurst KE, Parilla PA, Gennett T, Brown CM, et al. Outlook and challenges for hydrogen storage in nanoporous materials. Appl Phys A 2016;122:151.
[3] Mortazavi SZ, Reyhani A, Mirershadi S. Hydrogen storage properties of multi-walled carbon nanotubes and carbon nano-onions grown on single and bi-catalysts including Fe, Mo, Co and Ni supported by MgO. Int J Hydrogen Energy 2017;42:24885–96.
[4] Thornton AW, Simon CM, Kim J, Kwon O, Deeg KS, Konstas K, et al. Materials genome in action: identifying the performance limits of physical hydrogen storage. Chem Mater 2017;29:2844–54.
[5] Wang F, Zhang T, Hou X, Zhang W, Zhang J. Li-decorated porous graphene as a high-performance hydrogen storage material: a first-principles study. Int J Hydrogen Energy 2017;42:10099–108.
[6] Zou L, Zhou HC. Hydrogen storage in metal-organic frameworks. In: Chen YP, Bashir S, Liu J, editors. Nanostructured materials for next-generation energy storage and conversion - hydrogen production, storage, and

utilization; chap. 5. Berlin, Heidelberg: Springer-Verlag; 2017. p. 143–70.
[7] Ozturk Z, Baykasoglu C, Kirca M. Sandwiched graphene-fullerene composite: a novel 3-d nanostructured material for hydrogen storage. Int J Hydrogen Energy 2016;41:6403–11.
[8] Sethia G, Sayari A. Activated carbon with optimum pore size distribution for hydrogen storage. Carbon 2016;99:289–94.
[9] Ting VP, Ramirez-Cuesta AJ, Bimbo N, Sharpe JE, Noguera-Diaz A, Presser V, et al. Direct evidence for solid-like hydrogen in a nanoporous carbon hydrogen storage material at supercritical temperatures. ACS Nano 2015;9:8249–54.
[10] Wróbel-Iwaniec I, Díez N, Gryglewicz G. Chitosan-based highly activated carbons for hydrogen storage. Int J Hydrogen Energy 2015;40:5788–96. https://doi.org/10.1016/j.ijhydene.2015.03.034.
[11] House SD, Vajo JJ, Ren C, Rockett AA, Robertson IM. Effect of ball-milling duration and dehydrogenation on the morphology, microstructure and catalyst dispersion in Ni-catalyzed MgH_2 hydrogen storage materials. Acta Mater 2015;86:55–68.
[12] Robledo CB, Rojas MI, Cámara O, Leiva EPM. First-principles studies concerning optimization of hydrogen storage in nanoporous reduced graphite oxide. Int J Hydrogen Energy 2014;39:4396–403.
[13] Getman RB, Bae YS, Wilmer CE, Snurr RQ. Review and analysis of molecular simulations of methane, hydrogen, and acetylene storage in metal-organic frameworks. Chem Rev 2012;112:703–23.
[14] Suh MP, Park HJ, Prasad TK, Lim DW. Hydrogen storage in metal-organic frameworks. Chem Rev 2012;112:782–835.
[15] Kunowsky M, Marco-Lozar JP, Oya A, Linares-Solano A. Hydrogen storage in CO_2-activated amorphous nanofibers and their monoliths. Carbon 2012;50:1407–16.
[16] Cabria I, López MJ, Alonso JA. Hydrogen storage in nanoporous carbon. In: Sattler KD, editor. Handbook of nanophysics: functional nanomaterials; chap. 41. Boca Raton: CRC Press; 2010. 41–1, 41–16.
[17] Gogotsi Y, Portet C, Osswald S, Simmons JM, Yildirim T, Laudisio G, et al. Importance of pore size in high-pressure hydrogen storage by porous carbons. Int J Hydrogen Energy 2009;34:6314–9.
[18] Suárez-García F, Vilaplana-Ortego E, Kunowsky M, Kimura M, Oya A, Linares-Solano A. Activation of polymer blend carbon nanofibres by alkaline hydroxides and their hydrogen storage performances. Int J Hydrogen Energy 2009;34:9141–50.
[19] Phillips AB, Shivaram BS. High capacity hydrogen absorption in transition metal-ethylene complexes observed via nanogravimetry. Phys Rev Lett 2008;100:105505.
[20] Jordá-Beneyto M, Lozano-Castelló D, Suárez-García F, Cazorla-Amorós D, Linares-Solano A. Advanced activated carbon monoliths and activated carbons for hydrogen storage. Microporous Mesoporous Mat 2008;112:235–42.
[21] Smardz L, Jurczyk M, Smardz K, Nowak M, Makowieck M, Okonska I. Electronic structure of nanocrystalline and polycrystalline hydrogen storage materials. Renew Energy 2008;33:201–10.
[22] McKeown NB, Budd PM, Book D. Microporous polymers as potential hydrogen storage materials. Macromol Rapid Commun 2007;28:995–1002.
[23] Jordá-Beneyto M, Suárez-García F, Lozano-Castelló D, Cazorla-Amorós D, Linares-Solano A. Hydrogen storage on chemically activated carbons and carbon nanomaterials at high pressures. Carbon 2007;45:293–303.
[24] Yushin G, Dash R, Jagiello J, Fischer JE, Gogotsi Y. Carbide-derived carbons: effect of pore size on hydrogen uptake and heat of adsorption. Adv Funct Mater 2006;16:2288–93.
[25] McKeown NB, Ghanem B, Msayib KJ, Budd PM, Tattershall CE, Mahmood K, et al. Towards polymer-based hydrogen storage materials: engineering ultramicroporous cavities within polymers of intrinsic microporosity. Angew Chem Int Ed 2006;45:1804–7.
[26] Gogotsi Y, Dash RK, Yushin G, Yildirim T, Laudisio G, Fischer JE. Tailoring of nanoscale porosity in carbide-derived carbons for hydrogen storage. J Am Chem Soc 2005;127:16006–7.
[27] Challet S, Azaïs P, Pellenq RJM, Isnard O, Soubeyroux JL, Duclaux L. Hydrogen adsorption in microporous alkali-doped carbons (activated carbons and single wall nanotubes). J Phys Chem Solids 2004;65:541–4.
[28] Gogotsi Y, Nikitin A, Ye H, Zhou W, Fischer JE, Yi B, et al. Nanoporous carbide-derived carbon with tunable pore size. Nat Mater 2003;2:591–4.
[29] Rosi N, Eckert J, Eddaoudi M, Vodak DT, Kim J, O'Keeffe M, et al. Hydrogen storage in microporous metal-organic frameworks. Science 2003;300:1127–9.
[30] Pandey R, Rao BK, Jena P, Blanco MA. Electronic structure and properties of transition metal-benzene complexes. J Am Chem Soc 2001;123:3799.
[31] Bernard P, Chahine R. Determination of the adsorption isotherms of hydrogen on activated carbons above the critical temperature of the adsorbate over wide temperature and pressure ranges. Langmuir 2001;17:1950–5.
[32] Hailian L, Eddaoudi M, O'Keeffe M, Yaghi OM. Design and synthesis of an exceptionally stable and highly porous metal-organic framework. Nature 1999;402:276–9.
[33] Du K, Wang X, Liu Y, Hu P, Utama MIB, Gan CK, et al. Weak Van der Waals stacking, wide-range band gap, and raman study on ultrathin layers of metal phosphorus trichalcogenides. ACS Nano 2016;10:1738–43.
[34] Liu J, Li XB, Wang D, Lau WM, Peng P, Liu LM. Diverse and tunable electronic structures of single-layer metal phosphorus trichalcogenides for photocatalytic water splitting. J Chem Phys 2014;140:054707.
[35] Liu Q, Zhou W, Gao C, Hu T, Zhao X. Synthesis and second-order optical nonlinearity of DAMS/$Mn_2P_2S_6$. Chem Phys Lett 2009;477:388.
[36] Choudary BM, Madhi S, Chowdari NS, Kantam ML, Sreedhar B. Layered double hydroxide supported nanopalladium catalyst. J Am Chem Soc 2002;124:14127.
[37] Ulloa C, Troncoso RE, Bender SA, Duine RA, Nunez AS. Piezospintronic effect in honeycomb antiferromagnets. Phys Rev B 2017;96:104419.
[38] Lee S, Choi KY, Lee S, Park BH, Park JG. Tunneling transport of mono- and few-layers magnetic van der Waals $MnPS_3$. Apl Mater 2016;4:086108.
[39] Li X, Wu X, Yang J. Half-metallicity in $mnpse_3$ exfoliated nanosheet with carrier doping. J Am Chem Soc 2014;136:11065–9.
[40] Xiang H, Xu B, Xia Y, Ying J, Liu Z. Tunable electronic structures in MPX_3 (M = Zn, Cd; X = S, Se) monolayers by strain engineering. RSC Adv 2016;6:89901.
[41] Takano Y, Arai N, Arai A, Takahashi Y, Takase K, Sekizawa K. Magnetic properties and specific heat of MPS_3 (M=Mn, Fe, Zn). J Magn Magn Mater 2004;272–276:e593–5.
[42] Mirabal N, Lavayen V, Benavente E, Ana MS, González G. Synthesis, functionalization, and properties of intercalation compounds. Microelectr J 2004;35:37–40.
[43] Fogg AM, Green VM, O'Hare D. Superconducting metallocene intercalation compounds of b-ZrNCl. Chem Mater 1999;11:216–7.
[44] El-Meligi AA, Ismail NA, Madian M. Characterizing layered structure of $MgPS_3$ and new application as a hydrogen storage material. Int J Nanoparticles 2011;4:326–35.

[45] Ismail N, Temerk YM, El-Meligi AA, Badr MA, Madian M. Synthesis and characterization of $MnPS_3$ for hydrogen sorption. J Solid State Chem 2010;183:984–7.
[46] Ismail N, El-Meligi AA, Temerk YM, Madian M. Synthesis and characterization of layered $FePS_3$ for hydrogen uptake. Int J Hydrogen Energy 2010;35:7827–34.
[47] DiLabio GA, de la Roza AO. Noncovalent interactions in density functional theory, vol. 29. Hoboken, NJ: John Wiley & Sons; 2016. https://doi.org/10.1002/9781119148739.ch1.
[48] Klimeš J, Michaelides A. Perspective: advances and challenges in treating van der Waals dispersion forces in density functional theory. J Chem Phys 2012;137:120901.
[49] Rzepka M, Lamp P, de la Casa-Lillo MA. Physisorption of hydrogen on microporous carbon nanotubes. J Phys Chem B 1998;102:10894–8.
[50] Wang Q, Johnson JK. Hydrogen adsorption on graphite and in carbon slit pores from path integral simulations. Mol Phys 1998;95:299–309.
[51] Wang Q, Johnson JK. Molecular simulation of hydrogen adsorption in single-walled carbon nanotubes and idealized carbon slit pores. J Chem Phys 1999;110:577–86.
[52] Patchkovskii S, Tse JS, Yurchenko SN, Zhechkov L, Heine T, Seifert G. Graphene nanostructures as tunable storage media for molecular hydrogen. Proc Natl Acad Sci U. S. A 2005;102:10439–44.
[53] Garberoglio G, Skoulidas AI, Johnson JK. Adsorption of gases in metal organic materials: comparison of simulations and experiments. J Phys Chem B 2005;109:13094–103.
[54] Yildirim T, Hartman MR. Direct observation of hydrogen adsorption sites and nanocage formation in metal-organic frameworks. Phys Rev Lett 2005;95:215504.
[55] Samanta A, Furuta T, Li J. Theoretical assessment of the elastic constants and hydrogen storage capacity of some metal-organic framework materials. J Chem Phys 2006;125:084714.
[56] Cabria I, López MJ, Alonso JA. The optimum average nanopore size for hydrogen storage in carbon nanoporous materials. Carbon 2007;45:2649–58.
[57] Mpourmpakis G, Froudakis GE. Assessing the density functional theory in the hydrogen storage problem. J Nanosci Nanotechnol 2008;8:3091–6.
[58] Cabria I, López MJ, Alonso JA. Hydrogen storage in pure and Li-doped carbon nanopores: combined effects of concavity and doping. J Chem Phys 2008;128:144704.
[59] Cabria I, López MJ, Alonso JA. Hydrogen storage capacities of nanoporous carbon calculated by density functional and Møller-Plesset methods. Phys Rev B 2008;78:075415.
[60] Kuc A, Heine T, Seifert G, Duarte HA. H_2 adsorption in metal-organic frameworks: dispersion or electrostatic interactions? Chem Eur J 2008;14:6597–600.
[61] Kuc A, Heine T, Seifert G, Duarte HA. On the nature of the interaction between H_2 and metal-organic frameworks. Theor Chim Acta 2008;120:543–50.
[62] Ihm Y, Cooper VR, Peng L, Morris JR. The influence of dispersion interactions on the hydrogen adsorption properties of expanded graphite. J Phys Condens Matter 2012;24:424205.
[63] Alonso JA, Cabria I, López MJ. Simulation of hydrogen storage in porous carbons. J Mater Res 2013;28:589–604.
[64] Tang C, Chen S, Zhu W, Zhang A, Zhang K, Liu M. The high-capacity hydrogen storage abilities of the Ti atoms coated $Si@Al_{12}$ clusters. Chem Phys Lett 2013;586:116–20.
[65] Li XH, Ju XH. Density functional theory study on $(Mg(BH_4))_n$ (n = 1-4) clusters as a material for hydrogen storage. Comp Theor Chem 2013;1025:46–51.
[66] Wu YY, Zhao FQ, Ju XH. DFT study on structure and stability of $MgB_n^{\pm m}$ clusters. Comp Theor Chem 2014;1027:151–9.
[67] Tylianakis E, Dimitrakakis GK, Martín-Martínez FJ, Melchor S, Froudakis GE. Designing novel nanoporous architectures of carbon nanotubes for hydrogen storage. Int J Hydrogen Energy 2014;39:9825–9.
[68] Reshaka AH. DFT calculations for the electronic structure of alpha phase of $CsMgH_3$ as advanced hydrogen storage materials. Int J Hydrogen Energy 2016;41:2762–70.
[69] Cabria I, López MJ, Alonso JA. Simulation of the hydrogen storage in nanoporous carbons with different pore shapes. Int J Hydrogen Energy 2011;36:10748–59.
[70] Genovese L, Neelov A, Goedecker S, Deutsch T, Ghasemi SA, Willand A, et al. Daubechies wavelets as a basis set for density functional pseudopotential calculations. J Chem Phys 2008;129:014109.
[71] Deutsch T, Genovese L. Wavelets for electronic structure calculations. Collect SFN 2011;12:33–76.
[72] Website of the BigDFT Code; http://bigdft.org. [Accessed 5 August 2017].
[73] Perdew JP, Burke K, Ernzerhof M. Generalized gradient approximation made simple. Phys Rev Lett 1996;77:3865–8.
[74] von Lilienfeld OA, Tavernelli I, Rothlisberger U, Sebastiani D. Optimization of effective atom centered potentials for London dispersion forces in density functional theory. Phys Rev Lett 2004;93:153004.
[75] von Lilienfeld OA, Tavernelli I, Rothlisberger U, Sebastiani D. Performance of optimized atom-centered potentials for weakly bonded systems using density functional theory. Phys Rev B 2005;71:195119.
[76] Tapavicza E, Lin IC, von Lilienfeld OA, Tavernelli I, Coutinho-Neto MD, Rothlisberger U. Weakly bonded complexes of aliphatic and aromatic carbon compounds described with dispersion corrected density functional theory. J Chem Theory Comput 2007;3:1673–9.
[77] Lin I, Coutinho-Neto MD, Felsenheimer C, von Lilienfeld OA, Tavernelli I, Rothlisberger U. Library of dispersion-corrected atom-centered potentials for generalized gradient approximation functionals: elements H, C, N, O, He, Ne, Ar, and Kr. Phys Rev B 2007;75:205131.
[78] Library of Dispersion-Corrected Atom-Centered Potentials; http://lcbc.epfl.ch/page-71135-en.html. [Accessed 5 August 2017].
[79] Klingen W, Ott R, Hahn H. Über die Darstellung und Eigenschaften von Hexathio- und Hexaselenohypodiphosphaten. Z Anorg Allg Chem 1973;396:271–8.
[80] Brec R, Schleich DM, Ouvrard G, Louisy A, Rouxel J. Physical properties of lithium intercalation compounds of the layered transition chalcogenophosphates. Inorg Chem 1979;18:1814–8.
[81] Ouvrard G, Brec R, Rouxel J. Structural determination of some MPS_3 layered phases (M = Mn, Fe, Co, Ni and Cd). Mat Res Bull 1985;20:1181–9.
[82] Léaustic A, Audiére JP, Lacroix PG, Clément R. Synthesis, structural characterization, and physical properties of lamellar MPS_3 crystals intercalated with tetrathiafulvalene (M = Mn, Fe). Chem Mater 1996;7:1103–11.
[83] Hillman B, Norén L, Goossens D. Structural properties of compounds in the $MPS_{3-x}Se_x$ family. In: Micolich A, editor. Proceedings of the 35th annual Australian/New Zealand condensed matter and materials meeting. Australian Institute of Physics (AIP); 2011. p. 50–3.
[84] Flem GL, Brec R, Ouvard G, Louisy A, Segransan P. Magnetic interactions in the layer compounds $MPXR_3$, (M = Mn, Fe, Ni; X = S, Se). J Phys Chem Solids 1982;43:455–61.
[85] Broom DP. Hydrogen sorption properties of materials; chap. 3. London: Springer-Verlag; 2011. p. 61–116.

[86] Gross KJ, Carrington KR, Barcelo S, Karkamkar A, Purewal J, Parrilla P. Recommended best practices for the characterization of storage properties of hydrogen storage materials. Report to the Department of Energy Office of Energy Efficiency and Renewable Energy Hydrogen Storage Program under National Renewable Energy Laboratory Contract No. 147388. H2 Technology Consulting LLC; 2012. http://energy.gov/eere/fuelcells/downloads/recommended-best-practices-characterization-storage-properties-hydrogen-0. [Accessed 5 August 2017]. http://energy.gov/sites/prod/files/2014/03/f12/best_practices_hydrogen_storage.pdf.

[87] Ahn C, Purewal J. Storage materials based on hydrogen physisorption; chap. 7. CRC Press; 2016. p. 213–38.

[88] Madian M, Ismail N, El-Meligi AA. Layered chalcogenides for hydrogen storage. Germany: LAP: Lamber Academic Publishing; 2012.